Lawrence Berkeley National Laboratory

LBL Publications

Title

Integrated linker-regulation and ring-fusion engineering for efficient additive-free non-fullerene organic solar cells

Permalink

https://escholarship.org/uc/item/1q41991h

Journal

Journal of Materials Chemistry C, 8(36)

ISSN

2050-7526

Authors

Yin, Yuli

Zhang, Wenxia

Zheng, Zhi

et al.

Publication Date

2020-09-24

DOI

10.1039/d0tc02499f

Peer reviewed

eScholarship.org Powered by the California Digital Library
University of California

Integrated Linker-Regulation and Ring-Fusion Engineering towards High Efficiency Non-Fullerene Organic Solar cells

Yuli Yin,[#a,c] Wenxia Zhang,[#b] Zhi Zheng[a] Ziyi Ge,[b*] Yi Liu,[c*] Fengyun Guo,[a] Shiyong Gao,[a]

Liancheng Zhao,[a] Yong Zhang[a,d*]

[a] *School of Materials Science and Engineering, Harbin Institute of Technology, Harbin 150001, China. Email: yongzhang@hit.edu.cn*

[b] *Ningbo Institute of Materials Technology and Engineering, Chinese Academy of Sciences, Ningbo, 315201, China. Email: geziyi@nimte.ac.cn*

[c] *The Molecular Foundry, Lawrence Berkeley National Laboratory, Berkeley, California 94720, United States. E-mail: yliu@lbl.gov*

[d] *School of Materials Science and Engineering, Zhengzhou University, Zhengzhou 450001, China*

[#] Both authors contributed equally.

ABSTRACT

The rational molecular design and structural modification of the quasi-two-dimensional fused perylene diimide (quasi-2D FPDI) acceptors has received growing attention for the application in non-fullerene organic solar cells (NF-OSCs). Herein, we designed and synthesized two pairs of FPDI acceptors, one in the form of FPDI-π-bridge-FPDI with the π-bridge being either a thiophene (T) or thienothiophene (TT) unit, and the other being the corresponding ring-fusion counterpart. The four small molecule acceptors, namely T-FPDI, TT-FPDI, FT-FPDI and FTT-FPDI, were paired with the common PTB7-Th electron donor as the active materials for a comparative study of the effects of linkers and ring fusion on their photovoltaic performances. The T-FPDI-based NF-OSC gave a decent power conversion efficiency (PCE) of 5.50%, while a higher PCE of 7.17% with simultaneous enhancement of open circuit voltage (V_{oc}), short-circuit current density (J_{sc}) and fill factor (*FF*) was achieved for the TT-FPDI-based solar cells. The solar cells based on the ring-fused FT-FPDI and FTT-FPDI acceptors displayed a PCE of xx and 7.66%, both higher than the corresponding non-fused counterpart. Notably, the trade-off between the J_{sc} and V_{oc}, commonly observed in traditional fullerene OSCs, is alleviated in these systems. It is also worth noting that the NF-OSCs based on these fused perylene diimide acceptors do not need any solvent additives. The successful molecular engineering based on the novel quasi-2D FPDI building block may inspire the development of emergent electron acceptors for high performance additive-free NF-OSCs.

INTRODUCTON

Organic solar cells (OSCs) have progressed rapidly during the past decade with record high power conversion efficiencies (PCEs) reaching over 17% for single junction cells, making them viable candidates for commercial applications. The efficiency leap is largely due to the steady development of active materials, including both non-fullerene acceptors (NFAs) and matching polymer donors.[1] Especially notable is the emergence of small molecule non-fullerene acceptors (SMAs), thanks to the advances of rational molecular design incorporating electron-withdrawing building blocks.[2] Perylene diimide (PDI) and its derivatives are one of the most widely investigated electron-withdrawing building blocks for non-fullerene acceptors.[3] Their features, such as ease of functionalization, high electron affinity, suitable optoelectronic properties, as well as excellent thermo-stability, have established their competitiveness as ideal electron acceptors. One of the key challenges for this effort, however, lies in maintaining the balance between strong crystallinity, nanoscale phase separation and efficient charge transport ability in the blend films because of the strong propensity of aggregation related to the rigid polycyclic aromatic PDI core.[4] Encouragingly, fused perylenediimide dimer (FPDI) with quasi-two-dimensional (quasi-2D) geometry, firstly reported by Colin and Wang, [5] provides an effective way to address this challenge. Recent works have shown that the strong aggregation tendency of the PDI units can be significantly suppressed without adversely weakening the charge transport ability of the non-fullerene acceptors in such quasi-2D FPDI unit.[6] It has been shown that when two pairs of isomeric PDI and FPDI acceptors based on a FPDI-anthraquinone-FPDI

geometry were used as SMA for solar cells, both FPDI acceptors showed significantly higher PCEs relative to the PDI acceptors under the same device conditions (Figure 1).[7] These structural differences of the building blocks underlie the more favorable morphology compatibility and higher electron mobility of FPDI-based SMAs in the active layer than those of PDI-based SMAs. Additionally, a small amount of solvent additives has been generally introduced during the device fabrication for realizing the desired nanoscale morphology of the blends and enhancing the efficiency of PDI-based NF-OSCs.[8] According to the recently reported quasi-2D FPDI-based SMAs, it can be found that solvent additives play a minor role and even attenuate the device performance in these system, significantly streamlining the procedure and increasing the replicability.[9] It is of great significance to explore further structural variations of FPDI-based SMAs to delineate the structure-property relationship for constructing high-efficiency additive-free NF-OSCs.

Incorporating a conjugated linker or bridge to connect two or three PDI moieties in either a linear- or a star-shaped structure has become an effective strategy to modulate optical absorption, energy level, charge transport and crystallinity.[10] A series of quasi-2D FPDI systems and efficient SMAs were developed by adopting various linkers, such as bithiophene,[11] spirobifluorene,[9a] triphenylamine,[12] among others (Figure 1). These acceptors exhibited marked performance improvement, underscoring the effectiveness of the linker regulation strategy to optimize acceptor properties for higher photovoltaic performance. However, the effects of linkers with different steric hindrances and electron-donating ability on the charge transport, intermolecular

interactions as well as photovoltaic properties of FPDI acceptors are not well understood.

On the other hand, ring-fusion of PDI with donor aromatic unit attached on the bay position has been shown as an effective method for improving device efficiency over traditional PDI systems.[13] Xia et al. also studied the photovoltaic behavior of two star-shaped FPDI electron acceptors with non-fused and fused structures (Figure 1),[9c] which indicated that ring-fusion played a positive role in enhancing the device performance, consistent with the empirical molecular design of traditional PDI acceptors. Interestingly, another pair of conceptually similar FPDI acceptors,[11] in which two FPDI moieties were fused with the bithiophene bridge (Figure 1), provided a counterexample that the non-fused BT-FPDI device show higher efficiency than that of the fused fBT-FPDI. These results inspired us to investigate the effectiveness of ring fusion engineering in designed quasi-2D FPDI acceptor systems, taking into consideration of the role of linkers. Herein, two pairs of fused or non-fused acceptors based on FPDI building block and different conjugated linkers were synthesized, and their photovoltaic performance as SMAs were evaluated to understand such structural effects on molecular packing, charge transport, and device efficiency.

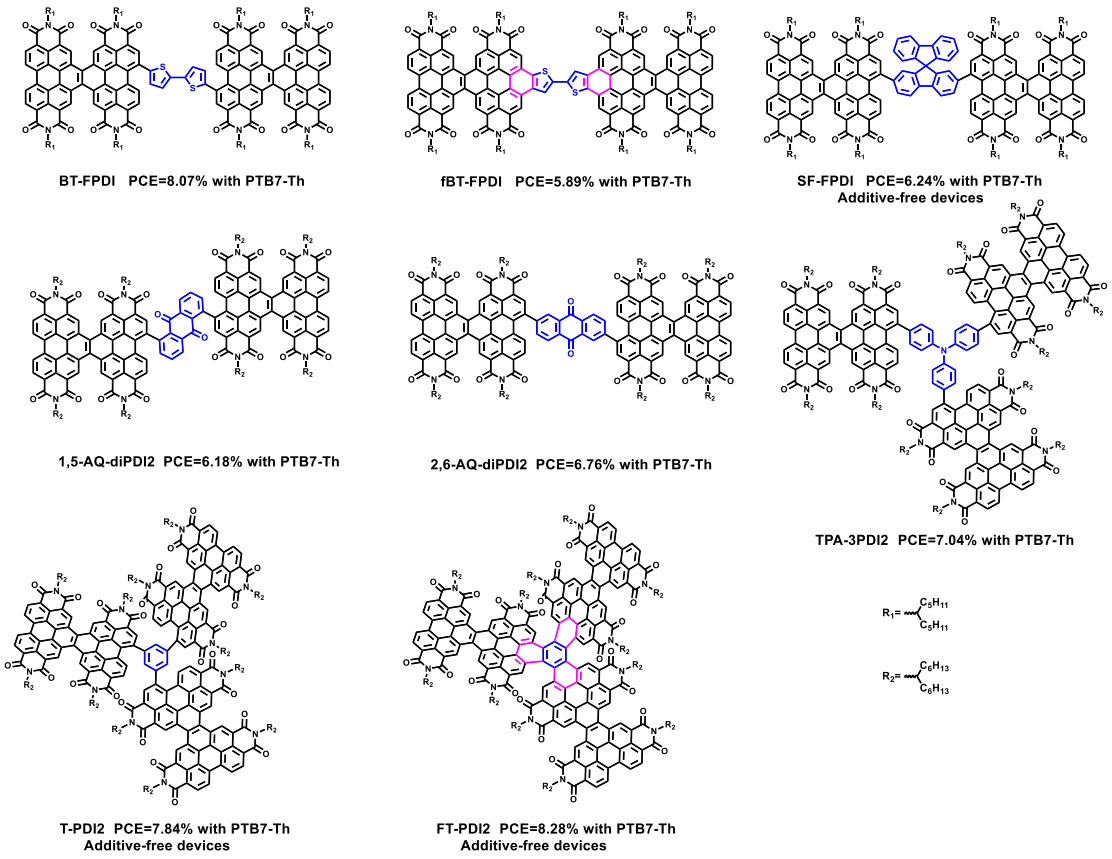

Figure 1. A list of recent examples of FPDI-based small molecule acceptors.

RESULTS AND DISCUSSION

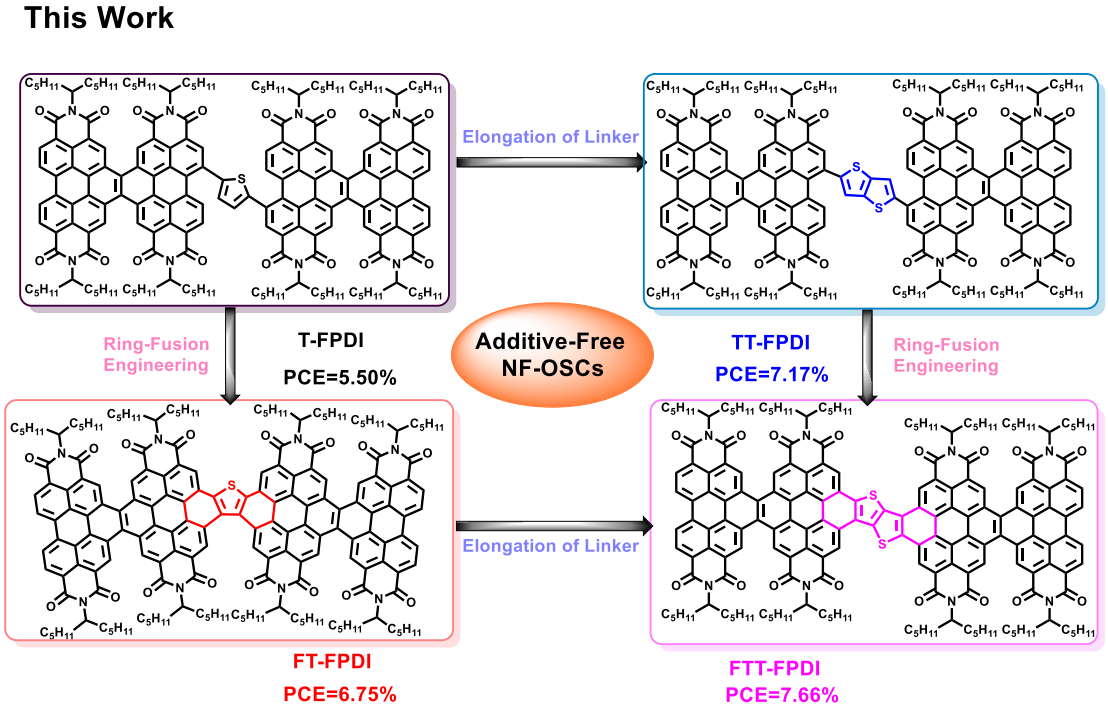

Figure 2. The chemical structures of four SMAs in this work.

The chemical structures of T-FPDI, TT-FPDI, FT-FPDI and FTT-FPDI were shown in Figure 2. T-FPDI and TT-FPDI were synthesized based on a palladium-catalyzed Stille coupling reaction in toluene, and the fused analogues, FT-FPDI and FTT-FPDI, were then obtained through photocyclization dehydrogenation reaction in high yield (over 80%). The synthetic details of these SMAs were described in Scheme S1 (Supporting Information). All SMAs were characterized by ^{1}H NMR spectroscopy, and were soluble in common organic solvents (e.g. dichloromethane, chloroform and chlorobenzene) at room temperature.

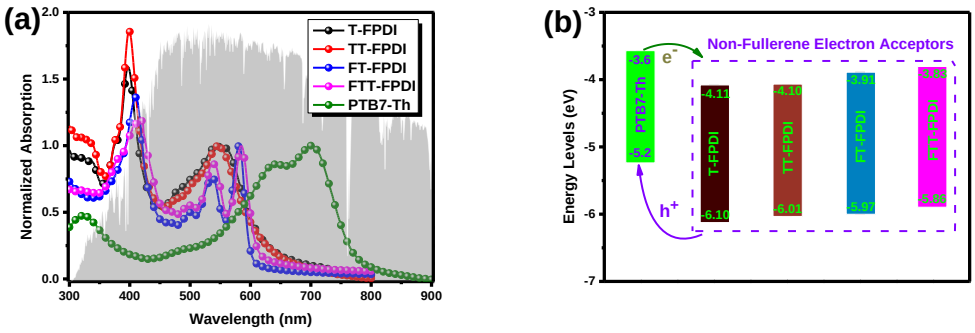

Figure 3. (a) Thin film UV-vis absorption spectra of the four SMAs; (b) the energy level diagram of these materials used in the NF-OSCs.

The optical properties of T-FPDI, TT-FPDI, FT-FPDI and FTT-FPDI in dichloromethane solution and in the solid state were investigated by UV-vis absorption spectroscopy, and the results were shown in Figure 3 and Table 1. In solution, T-FPDI and TT-FPDI displayed similar absorption profile with two pronounced absorption peaks located at 391 nm and 541 nm, attributable to the localized π-π* transition and intramolecular charge transfer (ICT) transition, respectively. As expected, a significant bathochromic shift of about 20 nm could be clearly observed in the spectra of the fused

counterparts. Two well-resolved 0-1 and 0-0 transition peaks centered at 527 nm and 578 nm for FT-FPDI, and 532 nm and 584 nm for FTT-FPDI (Figure S1a), respectively, were in accordance with an extended π conjugation due to ring fusion. Higher maximum extinction coefficients (1.1×10^5 M^{-1} cm^{-1} for FT-FPDI and 1.4×10^5 M^{-1} cm^{-1} for FTT-FPDI) were also observed (Table 1). Of note is that the absorption spectrum of FTT-FPDI showed a slightly bathochromic shift (~10 nm) relative to that of FT-FPDI in dichloromethane solution, resulted from the elongation of π-conjugation length. The absorption spectra of the four SMAs in the thin film state revealed (Figure 3a) a trend similar to that in the dichloromethane solution, but minimal red-shifts (~5-8 nm) of absorption peak were observed, hinting that intermolecular aggregation was suppressed despite the large π surface after ring annulation. From the absorption onsets of the thin films, the optical bandgaps of T-FPDI, TT-FPDI, FT-FPDI and FTT-FPDI were determined to be 1.99 eV, 1.91 eV, 2.06 eV, and 2.03 eV, respectively. The four SMAs films showed strong and broad absorption profiles at the region of 300-600 nm, complementary to that of the polymer donor (PTB7-Th) film which was in the range between 500 and 800 nm, a welcoming feature to achieve favorable photovoltaic performance. These optoelectronic properties clearly illustrated that the combined linker-regulation and ring-fusion strategy could greatly modulate the intra- and intermolecular interactions and optical properties of FPDI molecules, which may in turn play critical roles in achieving satisfactory charge transport and device performances in the NF-OSCs.

Table 1. Optical properties and frontier orbital energies of T-FPDI, TT-FPDI, FT-FPDI and FTT-

FPDI

SMAs	λ (nm)		ε_{max}^{sol}	λ_{onset}^{film}	E_g^{opt}	LUMO	HOMO
	Solution	Film	(M^{-1} cm^{-1})	(nm)	(eV)	(eV)[a]	(eV)[b]
T-FPDI	391/470/504/451	396/478/547	7.5×10^4	622	1.99	-4.11	-6.10
TT-FPDI	391/470/504/541	399/475/545	1.9×10^5	648	1.91	-4.01	-6.01
FT-FPDI	403/462/495/527/578	410/467/498/535/580	1.1×10^5	601	2.06	-3.91	-5.97
FTT-FPDI	413/464/493/532/584	417/466/500/538/584	1.4×10^5	610	2.03	-3.83	-5.86

[a]Measured from cyclic voltammetry. [b]Calculated from the electrochemical LUMO energy and optical band gap.

The electrochemical properties of the FPDI derivatives were studied by cyclic voltammetry (CV) measurements of the samples in thin film state, and the energy levels and the CV curves of these materials were provided in Figure 3b and Figure S1b. On the basis of the onset potentials and the optical band gaps, the HOMO/LUMO energy levels of T-FPDI and TT-FPDI were calculated to -6.10/-4.11 and -6.01/-4.01 eV, respectively (Figure 3b). The fused counterparts showed slightly raised LUMO energy levels (-3.91 eV for FT-FPDI and -3.83 eV for FTT-FPDI) relative to that of T-FPDI and TT-FPDI.

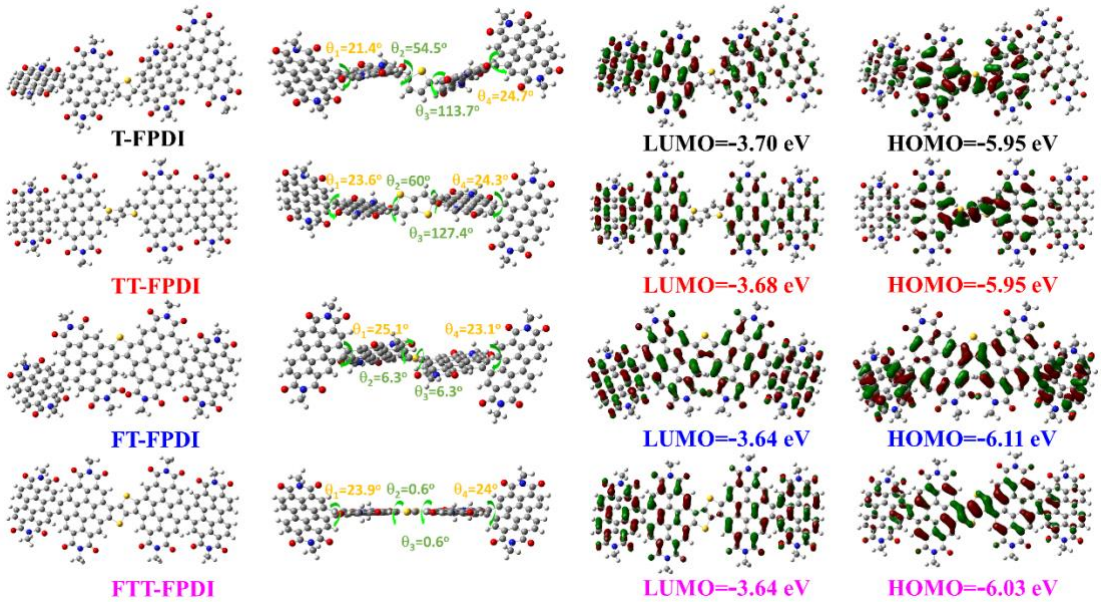

Figure 4. Top and side views of the optimized geometries and the calculated LUMO and HOMO

energy levels of four SMAs based on DFT calculations at the B3LYP/6-31G(d) level.

To further understand the difference between the molecular geometries and energy levels of these FPDI SMAs, theoretical calculations were carried out by running density functional theory (DFT) at the B3LYP/6-31G (d) level using the Gaussian 09 package. The long swallow-tail alkyl chains were replaced with methyl groups to simply the simulation. These calculations indicated a significant impact of the ring-fusion on the preferential conformation and the distribution of the frontier molecular orbitals, as shown in Figure 4. The FPDI unit showed dihedral angles of ~20° (θ_1 and θ_4 in Figure 4) between the two PDI subunits in all four molecules, which could effectively suppress the aggregation of PDI units. Additional non-planar twisting was observed in the conformation of both T-FPDI and TT-FPDI molecules, located between the FPDI and thiophene (T) or thieno[3,2-b]thiophene (TT) subunits. The dihedral angles between the two subunits in T-FPDI were calculated to be 54.5° and 66.3° (θ_2 and θ_3 in Figure 4), similar to that of TT-FPDI (60.0° and 53.6°), indicating significant steric repulsion between the aromatic protons from the linker unit and FPDI. After ring-fusion, such repulsion was significant eased, as indicated by the small (θ_2/θ_3 6.3°) in FT-FPDI, and in the case of FTT-FPDI, such dihedral angles were almost 0°. While it was apparent that the ring fusion eased the steric repulsion between FPDI and the central T or TT unit, it had little impact on the conformation of the FPDI units on each end of the molecules, as indicated by the fairly significant twisting and the dihedral angles (θ_1 and θ_4 ~20°). Such twisting dictated the intermolecular interactions and prevented these molecules from aggregation despite their large π surfaces, which was consistent with

the UV-vis absorption studies.

The electron distribution of frontier orbitals of the fully fused SMAs (FT-FPDI and FTT-FPDI) was also significantly altered in comparison to that of the non-fused SMAs (T-FPDI and TT-FPDI). As shown in Figure 4, there was little delocalization between the two FPDI units in the LUMO wave functions of T-FPDI and TT-FPDI. In contrast, the electron density was more spread across the overall π system in the fused FT-FPDI and FTT-FPDI, indicating enhanced electron delocalization between two FPDI units. Based on the modeling, wider energy band gap and higher lying LUMO levels were predicted for the fused FT-FPDI and FTT-FPDI, which were in accordance with the experimental results.

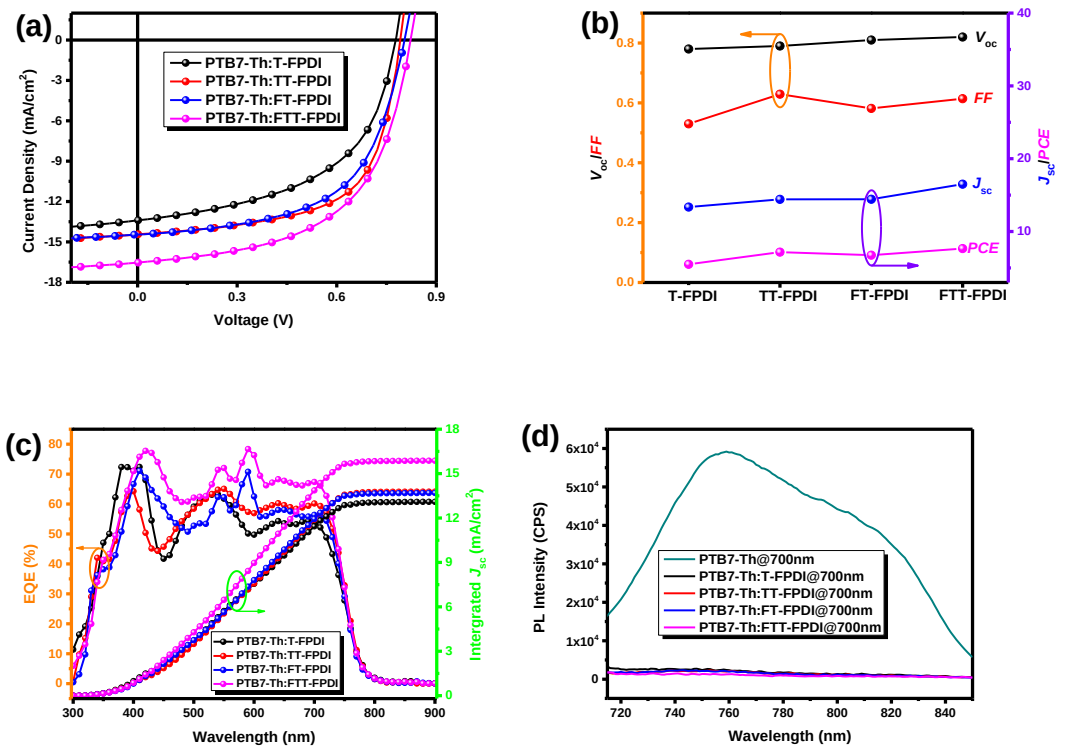

Figure 5. Device characteristics of the four additive-free solar cells based on different FPDI SMAs: (a) *J-V* curves ; (b) V_{oc}, J_{sc}, FF and PCE parameters; (c) EQE plots. (d) PL spectra of these blend

films and the pristine donor film excited at 700 nm.

The NF-OSCs devices were fabricated and characterized using a conventional configuration of ITO/PEDOT:PSS/photoactive layer/PDINO/Al, where PTB7-Th was used as the polymer donor, the FPDI-based SMA molecules as the electron acceptor, and PDINO as an electron transport layer. Similar to what we had found previously, [9a, 11] the optimal active material compositions were based on a PTB7-Th:SMA weight ratio of 1:1.5 and a total concentration of 20 mg/mL. To obtain the best device performance, device fabrication conditions were carefully optimized by tuning the different thermal annealing temperature and solvent additive, as shown in Table S1-S2. Amongst all the additive-treated devices, these with 0.5% DIO (volume ratio) gave the highest performance, which was essentially equivalent to that of the additive-free devices, suggesting that such additive was not necessary for FPDI-based devices. Therefore, no solvent additive treatment was exerted in subsequent device optimizations (Table S2). The characteristic current density-voltage (*J*-*V*) curves of these optimal devices based on PTB7-Th and SMAs blends were shown in Figure 5a, and the corresponding key photovoltaic parameters were summarized in Figure 5b and Table 2. The device based on T-FPDI yielded a PCE of 5.5%, with a V_{oc} of 0.78 V, a J_{sc} of 13.36 mA/cm^2, and a relatively low FF of 53.0%. When TT-FPDI was used as the SMA, the FF and PCE values of the corresponding device increased to 62.9% and 7.17%, respectively, with slightly enhanced V_{oc} (0.79 V) and J_{sc} values (14.42 mA/cm^2). Notably, the photovoltaic performances based on fused acceptors (FT-FPDI and FTT-FPDI) were significantly enhanced with simultaneously increased V_{oc} and J_{sc} relative

to that of the non-fused counterparts (T-FPDI and TT-FPDI), which could be ascribed to the upshifted LUMO levels and enhanced light absorption upon ring fusion engineering (Figure 5b). For the FT-FPDI based devices, the V_{oc} was increased to 0.81 V, together with a FF of 58.2% and an enhanced J_{sc} of 14.43 mA/cm^2, leading to a PCE of 6.75%. The champion PCE of 7.66% was achieved for the PTB7-Th:FTT-FPDI based additive-free device with a J_{sc} of 16.50 mA/cm^2, V_{oc} of 0.82 V, and FF of 61.4%. According to the equation $E_{loss} = E_g$-eV_{oc} (E_g is the optical bandgap of PTB7-th),[14] the energy losses of devices based on ring-fused FPDI acceptors (0.77 eV for FT-FPDI, 0.76 eV for FTT-FPDI) were smaller than those of the non-fused FPDI acceptors (0.80 eV for T-FPDI, 0.79 eV for TT-FPDI, as shown in Table 2).

The external quantum efficiencies (EQEs) of the PTB7-Th:SMAs optimal devices were plotted in Figure 5c. The integrated currents of the devices were in good agreement with these obtained from *J-V* measurements (Table 2). The optimized FT-FPDI and FTT-FPDI devices exhibited higher integrated current than the corresponding non-fused SMA devices, which was consistent with the higher EQE values in the range from 360 to 700 nm for the fused SMAs devices. The improved EQE response corroborated well with the enhanced absorption ability of SMAs upon ring fusion and improved charge transport. To examine the exciton dissociation and photoinduced charge-transfer properties, steady-state photoluminescent (PL) spectra of both pristine and blend films were obtained (Figure 5d). The emission peak at 759 nm of the pristine PTB7-th film was almost completely quenched (>95%) in all four blend films, indicating effective photoinduced hole transfer process from SMAs to PTB7-Th. In addition, the fused

acceptors-based blend films showed slight higher PL quenching efficiency (96.4% for FT-FPDI, 98.0% for FTT-FPDI) relative to that of the non-fused FPDI acceptors (95.8% for T-FPDI, 96.3% for TT-FPDI), suggesting more efficient exciton dissociation at D/A interfaces that also contributes to the higher PCE (Figure 5d).

Table 2. Photovoltaic performance parameters of the additive-free NF-OSCs under 1 Sun illumination (AM 1.5G, 100 mW/cm^2)

SMAs	V_{oc} **(V)**	J_{sc} **(mA/cm^2)[a)]**	**FF (%)**	**PCE (%)**	E_{loss} (eV)	μ_h **(cm^2 V^{-1} s^{-1})**	μ_e **(cm^2 V^{-1} s^{-1})**	μ_h/μ_e
T-FPDI	0.78	13.36 (13.10)[a]	53.0	5.5	0.80	1.99×10^{-4}	8.22×10^{-5}	2.42
TT-FPDI	0.79	14.42 (13.78)[a]	62.9	7.17	0.79	2.02×10^{-4}	1.04×10^{-4}	1.94
FT-FPDI	0.81	14.43 (13.70)[a]	58.2	6.75	0.77	4.93×10^{-4}	2.33×10^{-4}	2.12
FTT-FPDI	0.82	16.50 (15.87)[a]	61.4	7.66	0.76	5.67×10^{-4}	4.11×10^{-4}	1.38

[a] The values in parentheses are calculated from EQE.

To investigate the charge transport properties in the devices, charge carrier mobilities were examined in the blend thin films. The hole (μ_h) and electron (μ_e) mobilities were estimated by the space charge limited current (SCLC) method and the corresponding charge carrier mobilities were listed in Table 2. For the optimal PTB7-Th:T-FPDI blend, the calculated μ_h and μ_e were 1.99×10^{-4} cm^2 V^{-1} s^{-1} and 8.22×10^{-5} cm^2 V^{-1} s^{-1}, respectively, with a μ_h /μ_e ratio of 2.42. When using TT-FPDI to replace T-FPDI in the blend film, the respective hole and electron mobilities were enhanced to 2.02×10^{-4} cm^2 V^{-1} s^{-1} and 1.04×10^{-4} cm^2 V^{-1} s^{-1} with a more balanced μ_h /μ_e ratio of 1.94, which also correlated with the improvement of FF in the solar cells. The fused FPDI acceptors displayed further improved charge transport properties in the blend films relative to

these of the non-fused FPDI acceptors. As shown in Table 2, the PTB7-Th:FT-FPDI blend exhibited an electron mobility of 2.33×10^{-4} cm^2 V^{-1} s^{-1} while the PTB7-Th:FTT-FPDI blend gave the highest electron mobility of 4.11×10^{-4} cm^2 V^{-1} s^{-1}. Both blends showed higher hole transport mobilities, with the PTB7-Th:FTT-FPDI blend displaying a more balanced μ_h /μ_e ratio of 1.38. The dependence of photocurrent density (J_{ph}) on effective applied voltage (V_{eff}) was further investigated to understand the charge generation/extraction properties in the devices (Figure 6a). The photocurrent of all NF-OSCs saturated at a large reverse bias (V_{eff} 1-2 V), implying that almost all photogenerated electron-hole pairs were dissociated and the generated free carriers were collected at the electrodes.[15] The corresponding saturation photocurrents (J_{sat}) increased in the order of T-FPDI, TT-FPDI, FT-FPDI and FTT-FPDI, in accordance with the overall charge transport efficiency of the corresponding blends. The overall charge collection probability P(E,T), determined by the ratio of J_{ph}/J_{sat} under the short-circuit and maximum power conditions, can be used to evaluate the charge dissociation efficiency. As depicted in Figure 6a, the P(E,T) values were calculated to be 86.8%, 92.4%, 87.8%, and 91.0% for the T-FPDI, TT-FPDI, FT-FPDI and FTT-FPDI devices, respectively. The maximum exciton generation rate (G_{max}) of the solar cells were further calculated according to the equation $J_{sat} = qLG_{max}$. The NF-OSCs based on the non-fused T-FPDI and TT-FPDI acceptors showed G_{max} values of 9.26×10^{27} m^{-3} s^{-1} and 9.89×10^{27} m^{-3} s^{-1}, respectively, whereas higher G_{max} values of 9.90×10^{27} m^{-3} s^{-1} and 1.07×10^{28} m^{-3} s^{-1} were observed for the respective fused FT-FPDI and FTT-FPDI-based devices. The higher G_{max} values observed for the fused FPDIs than the non-fused ones

suggest that the ring fusion facilitates more efficient exciton generation and charge collection, which also correlates well with the more complementary absorption feature of the donor-acceptor blends.

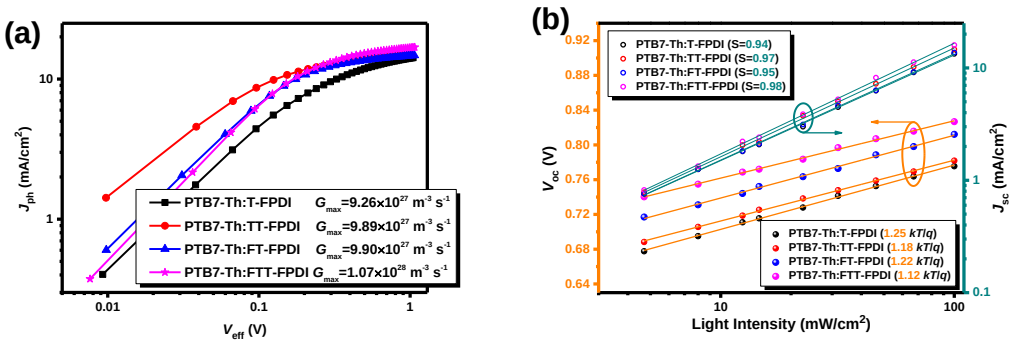

Figure 6. (a) J_{ph} versus V_{eff} curves and (b) plots of V_{oc} and J_{sc} against incident light intensity for the optimized NF-OSCs.

To gain deeper insight into the effect of linker-regulation and ring-fusion strategies on charge recombination of the optimal devices, the dependence of V_{oc} and J_{sc} on the light intensity (P_{light}) was carefully examined. The slope of the V_{oc}-P_{light} curves provided key information for the related recombination mechanism.[16] As shown in Figure 6b, the slope of the T-FPDI-based device (1.25 kT/q) was larger than that of the TT-FPDI-based device (1.18 kT/q), suggesting a more pronounced trap-assisted recombination in the PTB7-Th:T-FPDI-based device. On the other hand, the slope of the fully fused SMAs (1.22 kT/q for FT-FPDI and 1.12 kT/q FTT-FPDI) based devices was closer to the ideality factor (1 kT/q) relative to that of the non-fused devices, revealing that bimolecular recombination was more favorable than the trap-assisted recombination in the active layers containing ring-fused FPDIs. The correlation between J_{sc} and P_{light} was further investigated according to the power-law equation of $J_{sc} \propto P_{light}^{S}$.[17] Generally, if

the bimolecular recombination could be completely suppressed in the devices at short-circuit condition, the power law index (*S* value) will approach 1.[18] As shown in Figure 6b, the fully fused FT-FPDI and FTT-FPDI -based devices showed *S* values of 0.95 and 0.98, respectively, while that of the T-FPDI and TT-FPDI-based devices were more deviated from unity, indicating greater bimolecular recombination in the non-fused SMAs-based devices that were consistent with the observed lower current density and photovoltaic performance.

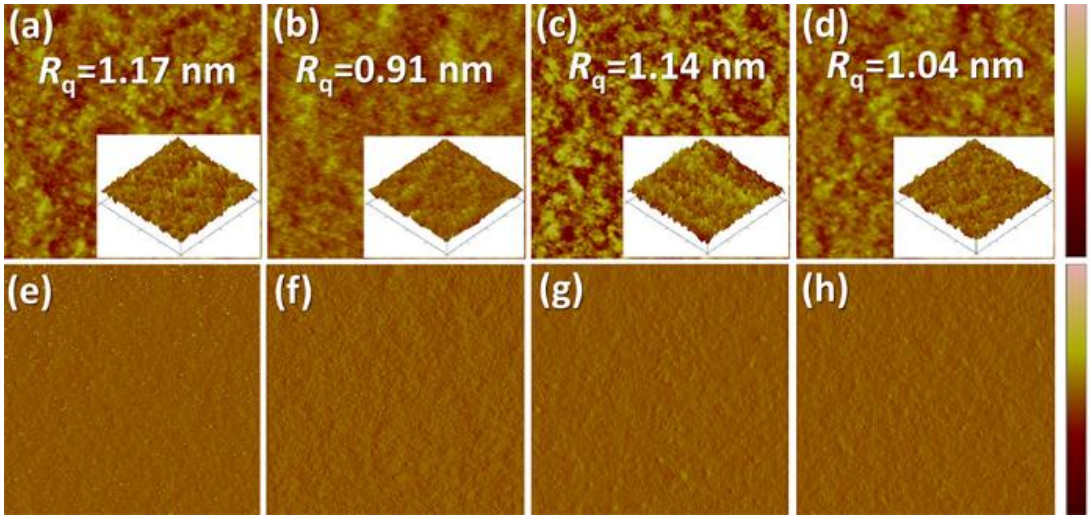

Figure 7. Atomic force microscopic (AFM) height (upper) and phase (lower) images of the optimal T-FPDI (a and e), TT-FPDI (b and f), FT-FPDI (c and g) and FTT-FPDI (d and h) blends.

Atomic force microscopy (AFM) height and phase images were acquired to examine the surface morphology and phase separation for the four active layers. The relevant images and the root-mean-square surface roughness (R_q) of all blends were shown in Figure 7. As revealed by the height images, the R_q values of T-FPDI-, TT-FPDI-, FT-FPDI-, and FTT-FPDI-based additive-free blends showed slight variations but were overall around 1 nm, The comparable surface roughness between the non-fused acceptors and the fused counterparts suggest similar aggregation behavior in the

blends regardless of the linker length and ring-fusion, which are consistent with the UV-vis studies.

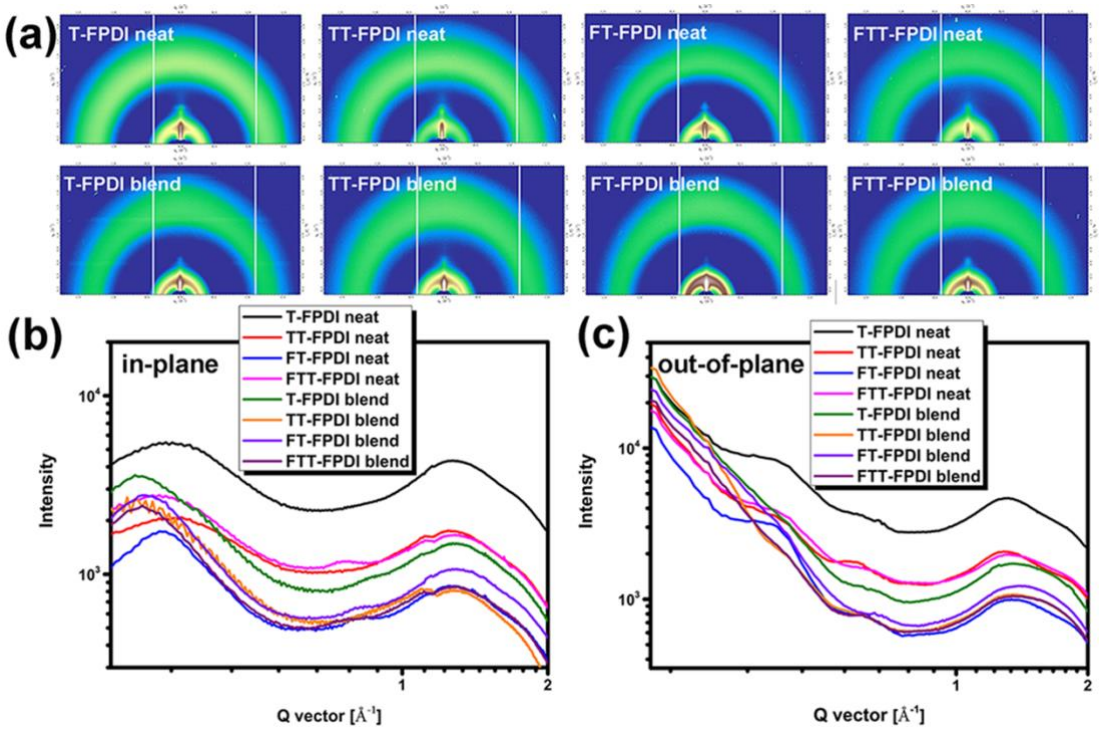

Figure 8. (a) 2D GIWAXS patterns for the neat and blend films, and 1D GIWAXS line-cut profiles of the corresponding films in the (b) in-plane and (c) out-of-plane directions.

Grazing-incidence wide-angle X-ray scattering (GIWAXS) measurement was performed to reveal the crystallinity and stacking behavior differences between the neat and blend films based on the four SMAs. The 2D GIWAXS patterns, together with the in-plane (IP) and out-of-plane (OOP) line-cut profiles of neat and blend films were shown in Figure 8. All neat and blend films displayed similar diffusive diffraction patterns with slightly more intensity in the OOP direction, indicating a random distribution of the crystallites with some preference towards edge-on orientation. The in-plane line-cuts of the neat films indicated peaks at q 0.32 $Å^{-1}$ and 1.26 $Å^{-1}$ for the four acceptors (T-FPDI, TT-FPDI, FT-FPDI and FTT-FPDI), corresponding to the inter-

lamellar *d*-spacing of 19.6 Å in the face-on oriented crystallites and alkly halo *d*-spacing of 4.99 Å, respectively. Ring-fusion slightly enhanced the crystallinity of FT-FPDI and FTT-FPDI neat films relative to that of the non-fused acceptors, evidenced by the appearance of a higher order peak in the IP direction. The OOP line-cuts of the neat films revealed multiple high order peaks, corresponding to edge-on lamella stacking of these acceptors. These features in the pristine films were still maintained in the blend films with the polymer donor PTB7-Th, suggesting the preservation of the molecular packing order in the blend. Despite these diffractive features, the thin films are in general quite amorphous considering the broad peak width and the lack of higher order peaks, indicating that intermolecular stacking in FPDI derivatives are greatly suppressed despite the ring fusion and the large π-surfaces. These findings are consistent with UV-vis results and the AFM studies.

Conclusion

In summary, a series of FPDI-based small molecule acceptors with different conjugated linkers were designed and synthesized for NF-OSCs. When using the elongated TT unit to bridge two quasi-2D FPDI units, the resulting TT-FPDI and FTT-FPDI acceptors displayed narrower band gaps and high electron mobilities relative to these bridged by a thiophene unit. The ring-fused acceptors show red-shifted absorption that is more complementary to the donor material, upshifted LUMO levels that is more beneficial for higher V_{OC}, and slightly higher crystallinity compared to the non-fused counterparts although intermolecular aggregation remains significantly suppressed due to the overall twisted, nonplanar geometry of FPDI units. The devices based on TT-

FPDI as electron acceptors exhibited a high PCE that the T-FPDI based devices. The photovoltaic performance can be further improved by synergistic effect of linker regulation and ring-fusion engineering, and the highest PCE of 7.66% was achieved in the ring-fused FTT-FPDI-based device without any additive treatment. This work demonstrated that integrating the effect of linker regulation and ring-fusion is a viable approach to improving the photovoltaic performance of quasi-2D FPDI-based electron acceptors.

ACKNOWLEDGMENTS

The authors acknowledge the support from the National Natural Science Foundation of China (21644006, and 51403044). Part of this work was performed as a user project at the Molecular Foundry, and the GIWAXS stdies were conducted at the Advanced Light Source, Lawrence Berkeley National Laboratory, all supported by the Office of Science, Office of Basic Energy Sciences, of the U.S. Department of Energy under contract no. DE-AC02-05CH11231. Y. Yin acknowledges the support from China Scholarship Council under Grant No. 201906120179. Y. Zhang thanks the support from the Fundamental Research Funds for the Central Universities (Harbin Institute of Technology).

Notes

The authors declare no competing financial interest.

REFERENCES

[1] a)J. Zhang, H. S. Tan, X. Guo, A. Facchetti, H. Yan, *Nature Energy* **2018**, *3*, 720; b)C. Yan, S. Barlow, Z. Wang, H. Yan, A. K. Y. Jen, S. R. Marder, X. Zhan, *Nat. Rev. Mater.* **2018**, *3*, 18003; c)H. Yao, J. Wang, Y.

Xu, S. Zhang, J. Hou, *Acc. Chem. Res.* **2020**; d)Y. Yin, Y. Zhang, L. Zhao, *Macromol. Rapid Commun.* **2018**, *39*, 1700697.

[2] a)L. Xiao, B. He, Q. Hu, L. Maserati, Y. Zhao, B. Yang, M. A. Kolaczkowski, C. L. Anderson, N. J. Borys, L. M. Klivansky, T. L. Chen, A. M. Schwartzberg, T. P. Russell, Y. Cao, X. Peng, Y. Liu, *Joule* **2018**, *2*, 2154; b)B. He, B. Yang, M. A. Kolaczkowski, C. A. Anderson, L. M. Klivansky, T. L. Chen, M. A. Brady, Y. Liu, *ACS Energy Letters* **2018**, *3*, 1028; c)H. Lai, Q. Zhao, Z. Chen, H. Chen, P. Chao, Y. Zhu, Y. Lang, N. Zhen, D. Mo, Y. Zhang, F. He, *Joule* **2020**, *4*, 688; d)Y. Cui, H. Yao, J. Zhang, K. Xian, T. Zhang, L. Hong, Y. Wang, Y. Xu, K. Ma, C. An, C. He, Z. Wei, F. Gao, J. Hou, *Adv. Mater.* **2020**, e1908205.

[3] a)A. Wadsworth, M. Moser, A. Marks, M. S. Little, N. Gasparini, C. J. Brabec, D. Baran, I. McCulloch, *Chem. Soc. Rev.* **2018**, *48*, 1596; b)C. Lee, S. Lee, G. U. Kim, W. Lee, B. J. Kim, *Chem. Rev.* **2019**, *119*, 8028; c)G. Li, S. Wang, D. Li, T. Liu, C. Yan, J. Li, W. Yang, Z. Luo, R. Ma, X. Wang, G. Cui, Y. Wang, W. Ma, L. Huo, K. Chen, H. Yan, B. Tang, *Solar RRL* **2020**, *4*, 1900453.

[4] a)G. Zhang, J. Feng, X. Xu, W. Ma, Y. Li, Q. Peng, *Adv. Funct. Mater.* **2019**, *29*, 1906587; b)H. Yin, Y. Geng, G.-Y. Sun, Z.-M. Su, *J. Phys. Chem. C* **2017**, *121*, 2125; c)Y. Yin, J. Song, F. Guo, Y. Sun, L. Zhao, Y. Zhang, *ACS Appl. Energy Mater.* **2018**, *1*, 6577.

[5] a)Y. Li, C. Wang, C. Li, S. Di Motta, F. Negri, Z. Wang, *Org. Lett.* **2012**, *14*, 5278; b)Y. Zhong, B. Kumar, S. Oh, M. T. Trinh, Y. Wu, K. Elbert, P. Li, X. Zhu, S. Xiao, F. Ng, M. L. Steigerwald, C. Nuckolls, *J. Am. Chem. Soc.* **2014**, *136*, 8122.

[6] a)Y. Yin, J. Yang, F. Guo, E. Zhou, L. Zhao, Y. Zhang, *ACS Appl. Mater. Interfaces* **2018**, *10*, 15962; b)Y. Yin, Z. Zheng, Y. Lu, D. Chen, M. Liu, F. Guo, S. Gao, L. Zhao, Y. Zhang, *ACS Appl. Mater. Inter.* **2019**, *11*, 29765; c)Y. Zhong, M. T. Trinh, R. Chen, W. Wang, P. P. Khlyabich, B. Kumar, Q. Xu, C.-Y. Nam, M. Y. Sfeir, C. Black, M. L. Steigerwald, Y.-L. Loo, S. Xiao, F. Ng, X. Y. Zhu, C. Nuckolls, *J. Am. Chem. Soc.* **2014**, *136*, 15215; d)Y. Zhong, M. T. Trinh, R. Chen, G. E. Purdum, P. P. Khlyabich, M. Sezen, S. Oh, H. Zhu, B. Fowler, B. Zhang, W. Wang, C.-Y. Nam, M. Y. Sfeir, C. T. Black, M. L. Steigerwald, Y.-L. Loo, F. Ng, X. Y. Zhu, C. Nuckolls, *Nat. Commun.* **2015**, *6*, 8242.

[7] X. You, J. Hu, M. Wu, H. Huang, G. Shao, J. Zhang, D. Wu, J. Xia, *Chemistry* **2019**, *25*, 12137.

[8] a)D. Meng, H. Fu, C. Xiao, X. Meng, T. Winands, W. Ma, W. Wei, B. Fan, L. Huo, N. L. Doltsinis, Y. Li, Y. Sun, Z. Wang, *J. Am. Chem. Soc.* **2016**, *138*, 10184; b)Y. Liu, C. Mu, K. Jiang, J. Zhao, Y. Li, L. Zhang, Z. Li, J. Y. Lai, H. Hu, T. Ma, R. Hu, D. Yu, X. Huang, B. Z. Tang, H. Yan, *Adv. Mater.* **2015**, *27*, 1015; c)H. Fu, Y. Wang, D. Meng, Z. Ma, Y. Li, F. Gao, Z. Wang, Y. Sun, *ACS Energy Letters* **2018**, *3*, 2729.

[9] a)Y. Yin, Z. Zheng, M. Liu, S. Gao, F. Guo, G. T. Mola, J. Wang, L. Zhao, Y. Zhang, *Dyes Pigments* **2020**, *175*, 108119; b)M. Wu, J.-P. Yi, J. Hu, P. Xia, H. Wang, F. Chen, D. Wu, J. Xia, *Journal of Materials Chemistry C* **2019**, *7*, 9564; c)M. Wu, J.-P. Yi, L. Chen, G. He, F. Chen, M. Y. Sfeir, J. Xia, *ACS Appl. Mater. Inter.* **2018**, *10*, 27894.

[10] a)C.-H. Wu, C.-C. Chueh, Y.-Y. Xi, H.-L. Zhong, G.-P. Gao, Z.-H. Wang, L. D. Pozzo, T.-C. Wen, A. K. Y. Jen, *Adv. Funct. Mater.* **2015**, *25*, 5326; b)A. Zhang, C. Li, F. Yang, J. Zhang, Z. Wang, Z. Wei, W. Li, *Angew. Chem.* **2017**, *56*, 1; c)X. Liu, T. Liu, C. Duan, J. Wang, S. Pang, W. Xiong, Y. Sun, F. Huang, Y. Cao, *J. Mater. Chem. A,* **2017**, *5*, 1713.

[11] Y. Yin, Z. Zheng, D. Chen, M. Liu, J. Zhang, F. Guo, S. Gao, L. Zhao, Y. Zhang, *J. Mater. Chem. A,* **2019**, *7*, 27493.

[12] J. Hu, X. Liu, K. Wang, M. Wu, H. Huang, D. Wu, J. Xia, *Journal of Materials Chemistry C* **2020**, *8*, 2135.

[13] a)H. Hu, Y. Li, J. Zhang, Z. Peng, L.-k. Ma, J. Xin, J. Huang, T. Ma, K. Jiang, G. Zhang, W. Ma, H. Ade, H. Yan, *Adv. Energy Mater.* **2018**, *8*, 1800234; b)J. Zhang, Y. Li, J. Huang, H. Hu, G. Zhang, T. Ma, P. C. Y.

Chow, H. Ade, D. Pan, H. Yan, *J. Am. Chem. Soc.* **2017**, *139*, 16092; c)H. Zhong, C.-H. Wu, C.-Z. Li, J. Carpenter, C.-C. Chueh, J.-Y. Chen, H. Ade, A. K.-Y. Jen, *Adv. Mater.* **2016**, *28*, 951.

[14] L. Zhan, S. Li, T.-K. Lau, Y. Cui, X. Lu, M. Shi, C.-Z. Li, H. Li, J. Hou, H. Chen, *Energy Environ. Sci.* **2020**, *13*, 635.

[15] W. Gao, M. Zhang, T. Liu, R. Ming, Q. An, K. Wu, D. Xie, Z. Luo, C. Zhong, F. Liu, F. Zhang, H. Yan, C. Yang, *Adv. Mater.* **2018**, *30*, 1800052.

[16] A. Zeng, M. Pan, B. Lin, T.-K. Lau, M. Qin, K. Li, W. Ma, X. Lu, C. Zhan, H. Yan, *Solar RRL* **2020**, *4*, 1900353.

[17] Y. Wu, Y. Zheng, H. Yang, C. Sun, Y. Dong, C. Cui, H. Yan, Y. Li, *Science China Chemistry* **2020**, *63*, 265.

[18] X. Han, J. Zhu, Y. Xiao, H. Jiang, Z. Zhang, J. Wang, Z. Li, Y. Lin, X. Lu, X. Zhan, *Solar RRL* **2020**, *n/a*, 2000108.